NANO LETTERS
Cite This: Nano Lett. 2018, 18, 1699−1706
Letter
pubs.acs.org/NanoLett

Thermoplasmonic Ignition of Metal Nanoparticles

Mehmet Mutlu,[†] Ju-Hyung Kang,[†] Søren Raza,[†] David Schoen,[†,‡] Xiaolin Zheng,[§] Pieter G. Kik,[†,∥] and Mark L. Brongersma*[,†]

[†]Geballe Laboratory for Advanced Materials, Stanford University, Stanford, California 94305, United States
[‡]Exponent Inc., Menlo Park, California 94025, United States
[§]Department of Mechanical Engineering, Stanford University, Stanford, California 94305, United States
[∥]CREOL, The College of Optics and Photonics, University of Central Florida, 4000 Central Florida Boulevard, Orlando, Florida 32816, United States

Supporting Information

ABSTRACT: Explosives, propellants, and pyrotechnics are energetic materials that can store and quickly release tremendous amounts of chemical energy. Aluminum (Al) is a particularly important fuel in many applications because of its high energy density, which can be released in a highly exothermic oxidation process. The diffusive oxidation mechanism (DOM) and melt-dispersion mechanism (MDM) explain the ways powders of Al nanoparticles (NPs) can burn, but little is known about the possible use of plasmonic resonances in NPs to manipulate photoignition. This is complicated by the inhomogeneous nature of powders and very fast heating and burning rates. Here, we generate Al NPs with well-defined sizes, shapes, and spacings by electron beam lithography and demonstrate that their plasmonic resonances can be exploited to heat and ignite them with a laser. By combining simulations with thermal-emission, electron-, and optical-microscopy studies, we reveal how an improved control over NP ignition can be attained.

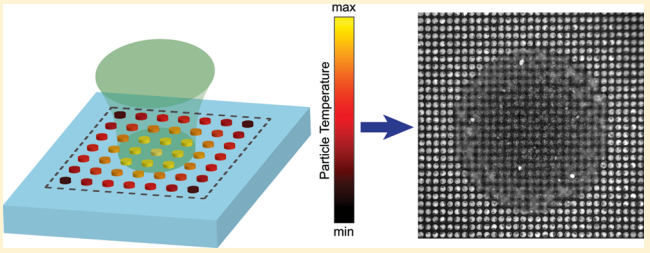

KEYWORDS: *Plasmonics, energetic materials, energy harvesting, laser processing*

Localized surface plasmon resonances (LSPRs) are charge density oscillations in a subwavelength metallic NP that are coupled to highly confined optical fields.[1] Recent advances in our understanding and control over localized heating of metal NPs[2−5] through the optical excitation of LSPRs has enabled many important applications, which include photothermal imaging,[6] nanosurgery,[7] drug delivery,[8] photothermal therapy,[9] microfluidics,[10] nanofiltration,[11] nanochemistry,[12] and plasmonic rulers.[13] Here, we propose to fuse the fields of plasmonics and energetic materials by leveraging decades of work on LSPRs to gain a new level of control and understanding of NP ignition.

The earth abundance, low cost, and large energy density of Al has propelled its use as an energetic material.[14] Its energy density (31 MJ/kg) is almost 2 orders of magnitude higher than that of a lithium-ion battery (0.4 MJ/kg). It is also easily patterned, nanostructured and integrated into portable microsystems.[15] For these reasons, it finds extensive use as a propellant, explosive, method of actuation, and as a source of on-board energy. Driven by a desire to increase the rate at which energy is released, researchers have discovered that Al nanostructures can offer significant advantages over their micron-sized counterparts, such as increased reactivity, a decreased ignition delay, and decreased ignition temperatures.[14] Aluminum nanostructures oxidize through distinct mechanisms that can be controlled by modifying the heating rate. Under slow heating conditions, oxidation occurs through the diffusive oxidation mechanism which involves the diffusion of Al and oxygen toward each other through a growing oxide shell.[16,17] Under fast heating conditions, on the other hand the nanostructures oxidize through the melt-dispersion mechanism.[18−21] The high heating rate (10^6−10^8 K/s) causes the Al core to melt and rapidly undergo a 6% volume expansion, which creates a pressure of several GPa. This pressure is sufficient to overload the native oxide shell with hoop stresses that exceed its ultimate strength, causing its dynamic spallation. The rapid removal of the oxide shell results in a tensile pressure in the metallic core that exceeds the cavitation limit of liquid Al and causes it to disperse into a plurality of smaller clusters that then can rapidly oxidize to produce a massive amount of heat.

External illumination provides a convenient and controlled method to achieve rapid heating and ignition of metal NPs from a remote location. Both lasers[22,23] and flash lamps[24,25] have been used to ignite Al nanopowders. These studies have hinted at the possible role of LSPRs in accelerating the ignition and oxidation processes, but the inhomogeneous nature of the samples and the fast heating/burning rates have prevented the collection of conclusive evidence. It is clear that systematic ignition studies on engineered NP samples could help elucidate the role of plasmons

Received: November 8, 2017
Revised: December 29, 2017
Published: January 22, 2018

DOI: 10.1021/acs.nanolett.7b04739
Nano Lett. 2018, 18, 1699−1706

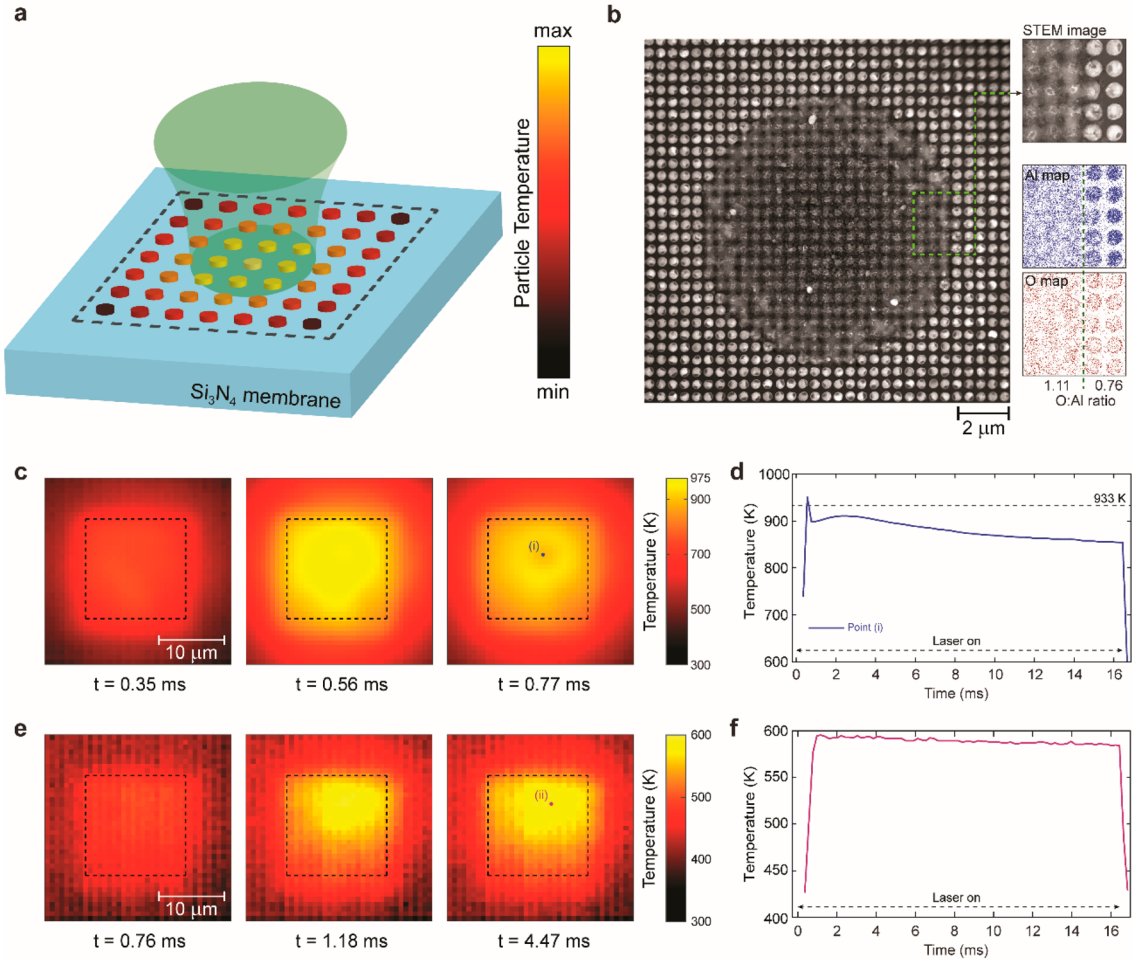

Figure 1. Observation of optically stimulated ignition in Al nanoparticle arrays. (a) Schematic of an ignition experiment using an array of Al nanoparticles fabricated on a 50 nm thick silicon nitride membrane. As a result of the partial absorption of the focused laser beam, particles are heated and a nonuniform temperature profile arises. For a sufficiently high laser power, ignition in the MDM regime can be stimulated. (b) STEM and EDS analysis of particles ignited via the MDM. The overview STEM image shows a circular region of almost completely dispersed particles. The brighter area in the array shows particles that were not ignited. The boundary between ignited and nonignited area is analyzed with EDS to create the displayed elemental maps for aluminum and oxygen. (c) Temperature profiles recorded at different instants using an infrared camera. The area contained by the dashed lines represents the square particle array. The laser is turned on at t = 0 for 16 ms using an electro-optic modulator. (d) Time trace of temperatures at point (i), the center of the laser beam. The horizontal line at 933 K represents the threshold temperature for triggering MDM. (e) Infrared camera images captured using a laser power not sufficiently high to trigger the MDM. (f) Time trace of temperature at point (ii), the center of the laser beam. Because of the lower optical power used, the sudden temperature drop observed in (d), which is associated with the MDM based ignition of NPs, is nonexistent here. Temporal resolution of the camera is 206 μs.

and facilitate the development of nanoengineered energetic materials with improved ignition and burning properties. The present work aims to leverage a flurry of activity and increased knowledge about the plasmonic properties of Al nanoparticles to reach a new level of control over the MDM.[26]

Results and Discussion. To demonstrate the possibility of achieving the MDM on lithographically defined NPs, we first generate disk-shaped Al NPs on a 50 nm thin Si_3N_4 transmission electron microscope (TEM) membrane (Figure 1a). We start with an array of 400 nm diameter and 70 nm high NPs arranged in a square lattice with a pitch of 500 nm. At these dimensions, the particles support plasmonic resonances in the visible range.[26] We illuminate and heat the NPs by driving such resonances with a green laser (λ_0 = 532 nm) focused to produce a spot on the surface with an approximately Gaussian intensity distribution: $i(r) = i_o \exp\left(-\frac{r^2}{w^2}\right) = i_o \exp(-R^2)$, where w is the beam radius of about 2.2 μm (fwhm = 3.7 μm) and R is a normalized radius. The beam is turned on for a 16 ms duration using an electro-optic modulator. The incident radiation is absorbed selectively in the metallic core of the Al nanoparticles with negligible absorption in the transparent nitride membrane. This causes rapid heating of the nanoparticles, accompanied by heat dissipation into the membrane. The impact of a series of incident powers $P = i_0 \pi w^2$ is investigated in the range from 1−200 mW. Figure 1b show a scanning TEM (STEM) micrograph taken after a single laser pulse at power of 132 mW. NPs in the center of the illumination spot were physically removed from the substrate consistent with the MDM. The DOM has also been observed for lower powers/heating rates (Figure S1). Energy-dispersive X-ray spectroscopy (EDS) taken at the edge of the region where particle removal has taken place reveals more about the nature of the ignition, as shown in the inset of Figure 1b. Aluminum and oxygen atoms are seen to be dispersed across the ignition area including the regions between the original particle locations. We also find that the oxygen-to-aluminum atomic ratio just inside the ignition region

DOI: 10.1021/acs.nanolett.7b04739
Nano Lett. 2018, 18, 1699−1706

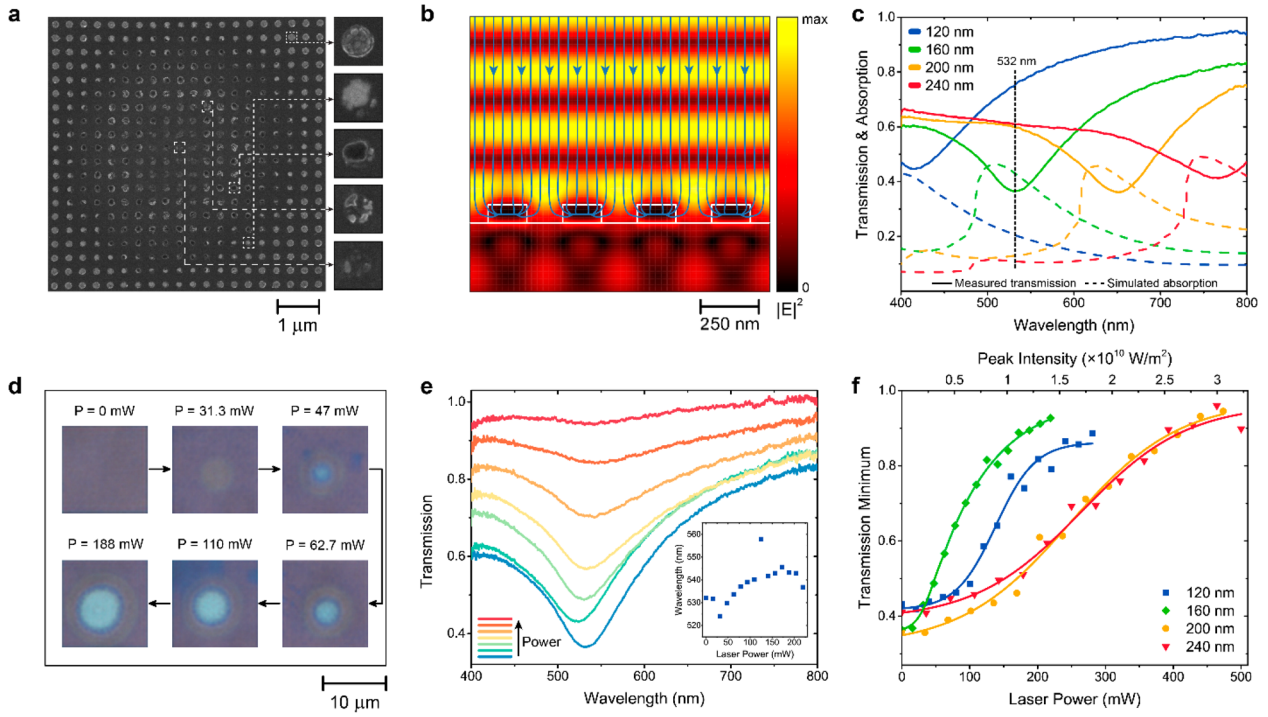

Figure 2. Optical control and characterization of the ignition process. (a) SEM image showing the occurrence of MDM-based ignition with Al nanoparticles fabricated on optically thick borosilicate glass. The zoomed versions of five particles shown on the right displays damage to a particle is most severe at the beam center and decreases with distance from it. Here, the pulse length is selected as 1 ms. (b) Cross-section of the simulated electric field intensity and flow of light as derived from the Poynting vector at the dipolar LSP resonance of an infinitely repeating array of Al disks. The cross-section is recorded on a plane that intersects a line of particles at their centers. (c) Measured transmission (solid lines) and simulated absorption (dashed lines) spectra for cylindrical aluminum NP arrays with different geometrical parameters. Experimentally and numerically observed resonance wavelengths extracted using the spectral locations of transmission dips and absorption peaks agree closely. (d) Optical microscope images showing the light transmission through arrays of 160 nm diameter Al NPs after illumination with increasing laser powers at a fixed pulse duration of 1 ms. A new array is illuminated for each image. (e) Transmission spectra measured after the application of 1 ms laser pulses to a 160 nm NP array with powers of 15.7, 31.3, 47, 63, 94, 157, and 219 mW. Transmitted light is collected from an area with a diameter of ~12 μm and centered at the laser beam center. The inset shows the spectral locations of transmission dips for various laser powers. (f) Traces of transmission minima for all particle sizes subsequent to the application of 1 ms laser pulses with varying powers.

is 1.11 compared to only 0.76 just outside the ignition region. These observations are consistent with the rapid dispersion of metal nanoparticulates (within milliseconds) and their subsequent oxidation, which are key signatures of the MDM.[21] The slower DOM operates at much longer (approximately 1 s) time scales[27] and would not have produced such high O levels.

We also record the ignition process with a fast, infrared thermal-camera (Figure 1c) to investigate whether the achieved temperatures and heating rates are consistent with the MDM. A maximum temperature of 975 K is recorded during the laser pulse (t = 0.77 ms). This is just above the melting temperature of bulk Al (T_M = 933 K). The temperature evolution in the center of the illumination area indicates that heating rates in excess of 10^6 K/s can be achieved, sufficient to trigger the MDM. At later times during the laser pulse, a sudden temperature drop occurs in the center of the illumination spot, which is linked to the ignition and removal of NPs that served as sources of heat. Such an anomalous temperature drop is nonexistent in similar experiments at lower laser powers where no NPs are removed (Figure 1e,f). After removal of the particles in the central region and the associated temperature drop, the temperature at the center subsequently increases more slowly via the inward diffusion of heat from the periphery where remaining metallic particles have not yet reached a steady state temperature. Finally a gradual drop in the temperature is observed, which is attributed to the oxidation of and reduced light absorption by NPs in the periphery, which occurs on a longer time scale.

Next, we move to NPs on thicker borosilicate glass slides, which are more practical and easy-to-manipulate substrates for a variety of optical studies. Figure 2a shows a scanning electron microscope (SEM) image of a NP array on an optically thick borosilicate glass substrate after exposure to a single 1 ms long laser pulse. Qualitatively similar results are seen as on the nitride membrane, where particles are almost completely removed in the center of the spot. Quantitative differences are expected based on the different thermal transport properties of this substrate and the fact that this type of glass can serve as a source of oxygen. Cross-sectional STEM results show material depletion in the glass under the aluminum particles in the central region (Figure S2). Clear spatial variations in the NP morphology can be observed in the SEM image going from the center of the spot to the periphery. These type of spatial variations are associated with the dependence of the MDM on temperature and heating rates. The laser pulse also causes a slight raise of the glass surface as seen in atomic force microscopy (Figure S3). This is attributed to the local heating of the glass above its glass transition temperature (~800 K)[28] and its volume expansion. Whereas lateral expansion of the material during the pulse is prevented by the surrounding colder material, plastic flow can occur in the direction normal to the sample surface during and immediately

DOI: 10.1021/acs.nanolett.7b04739
Nano Lett. 2018, 18, 1699−1706

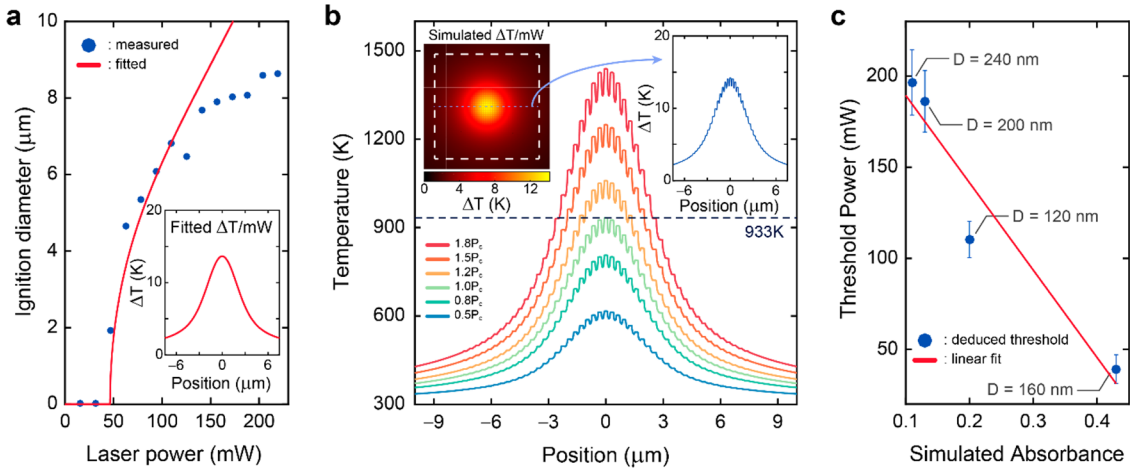

Figure 3. Thermal characterization of the ignition process. (a) Ignition region diameters for 160 nm particles as estimated from measurements of the transparent region diameters from optical microscope images taken after ignition. The fitted line follows from a simple model for the steady-state temperature, as explained in the main text. The inset shows the estimated temperature increase for 1 mW of laser power extracted from this model. Here, a position of zero corresponds to the beam center. (b) Simulated cross-sectional temperature profiles for a 160 nm diameter NP array for different laser powers. A threshold temperature of 933 K is assumed for ignition, whereas the ambient temperature is taken as 300 K. P_c is the laser power that heats the central particle to 933 K. The left inset shows the two-dimensional map of the simulated temperature increase for a power P = 1 mW. Boundaries of the array are denoted by the white dashed lines. The right inset shows the temperature increase profile along the indicated light-blue line. (c) Threshold power values obtained for all arrays by averaging the first laser power creating a nonzero ignition diameter and the power before this value. An error-bar is associated with each threshold power corresponding to the step size between consecutive measurements. A line is fitted to the data to highlight the negative correlation between NP absorbance and threshold laser power.

after the pulse.[29] This state of the sample is frozen in by the rapid cooling.

With the knowledge that laser pulses can initiate the MDM in nanopatterned Al NPs, we move to the question whether the ignition process can be optimized and controlled by tailoring their plasmonic properties. Figure 2b shows a simulation of the flow of green light (λ_0 = 532 nm) that is normally incident on an array of Al NPs with diameters and edge-to-edge spacing of 160 nm. The power flow distribution shows that the optical absorption cross-section of the NPs (from which light flows into the metal particles to be absorbed) can exceed their geometrical cross section. This indicates that a large percentage of the light (43%) can be absorbed in just a single layer of particles to achieve very effective energy deposition and heating. To explore the impact of the NP size on the absorption, we analyzed four square arrays containing Al disks featuring different diameters. The array periodicity for each sample was taken to be twice the disk diameter, thus keeping the filling fraction of metal constant. (and thus also the amount of metal per unit area heated by the laser pulses). Figure 2c shows the numerically obtained absorption spectra and experimentally measured transmission spectra for the fabricated arrays. The spectral location of the transmission dips and strong absorption peaks agree closely between simulations and experiments (see Figure S4 for simulation and Materials and Methods for experiment details). On the basis of this correspondence, these features can be associated with a dipolar localized surface plasmon resonance whose spectral excitation properties are modified from a simple Lorentzian through the occurrence of an evanescent diffractive order (i.e., Wood anomaly) that radiatively couples the particles.[30] In the following, we will exploit the tunability of this resonance to manipulate the ignition at a fixed excitation wavelength of λ_0 = 532 nm.

Figure 2d shows optical transmission measurements on 15 identical arrays that feature 160 nm diameter NPs and after ignition by a single laser pulse but with different illumination powers in the range from 0 mW to 188 mW. The spot radius (w = 2.2 μm) and pulse duration (t_p = 1.0 ms) are kept constant. The ignited area is seen to become more transparent and it expands in size with increasing laser power. SEM images as in Figure 2a show that the transparent areas correspond to regions where virtually all NP have been removed. To quantify the transmission changes, transmission spectra were measured from a circular region (diameter ~12 μm) at the center of the ignition region for each ignition power. The resulting spectra for 160 nm diameter NPs are shown for selected laser powers in Figure 2e. All spectra feature a broad transmission dip near 530 nm that is associated with the plasmon resonance of the NPs. The dip monotonically decreases in its prominence due to the expansion of the MDM ignited region. In addition to this transmission increase, small spectral shifts are observed as shown in the inset to Figure 2e for the transmission dips. These shifts may be attributed to refractive index changes in the glass during thermal cycling,[31] change in the NP shape and size due to partial dispersion, and a reduced radiative coupling between the NPs[32] in the array due to the removal of some NPs.[33] It should also be noted here that increasing the pulse length beyond 1 ms has a negligible effect on the ignition region diameter since most NPs inside the illumination spot are removed within 1 ms (Figure S5).

By repeating the measurements shown in Figure 2e for all four NP array geometries (Figure S6), we reveal the plasmon-enabled control over the ignition process. Figure 2f summarizes the obtained transmission minimum as a function of pulse energy for the four particle geometries, allowing for direct comparison of the ignition performance for different geometries. The 160 nm particles are seen to require the lowest power for ignition. This can be understood by noting that these NPs have their plasmon resonance wavelength closely matched to the laser wavelength (532 nm) and therefore absorb light most efficiently. The 120 nm diameter particles require a larger power, as expected based on their lower absorption at 532 nm (Figure 3c). Particles with 200 and 240 nm diameters each require similar laser power, as

DOI: 10.1021/acs.nanolett.7b04739
Nano Lett. 2018, 18, 1699−1706

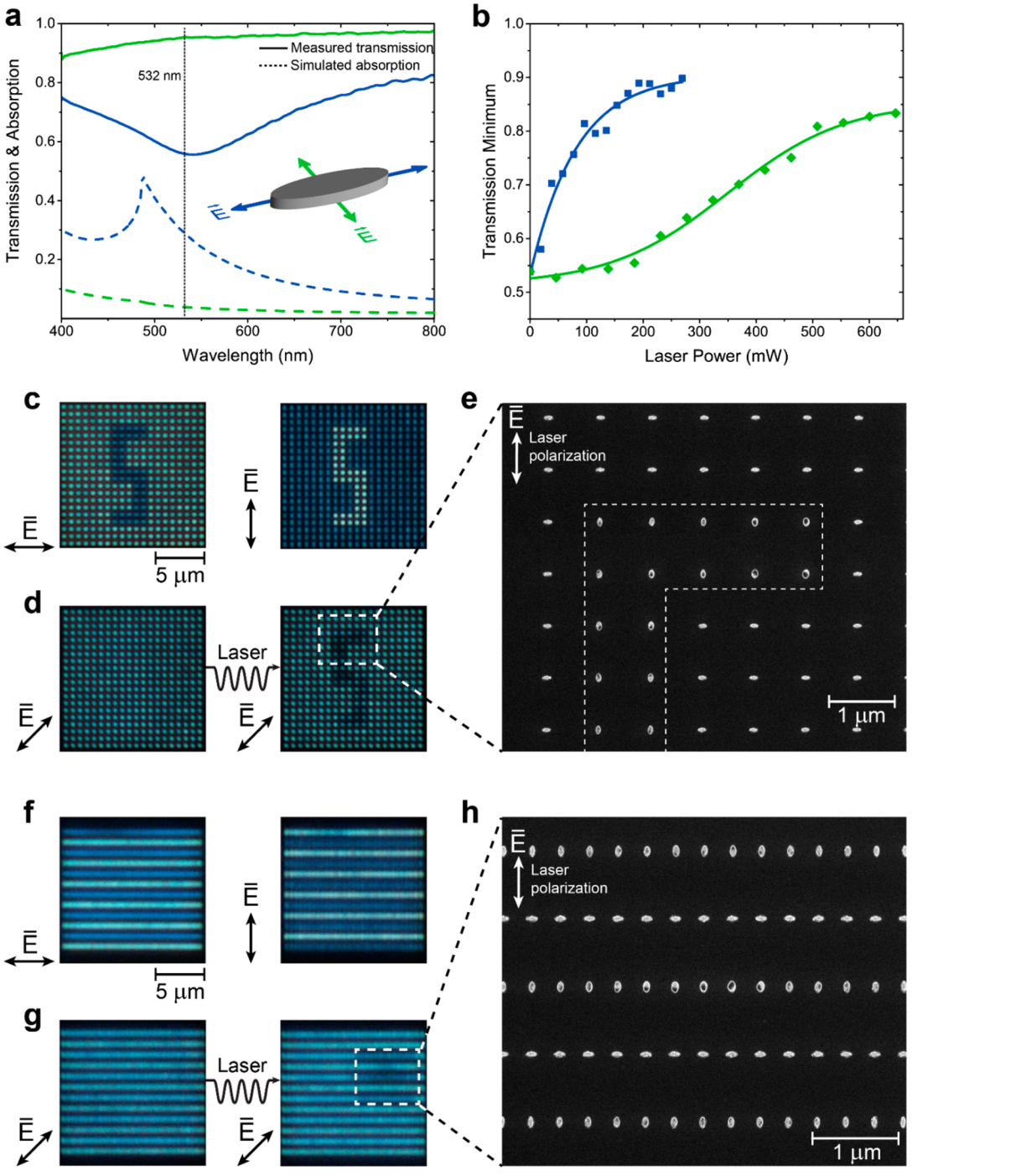

Figure 4. Polarization-dependent and submicron spatial control over nanoparticle ignition. (a) Measured transmission (solid lines) and simulated absorption (dashed lines) spectra for an elliptical aluminum NP array. Particles measure 50 and 125 nm along their short and long axes, respectively. They are arranged in a lattice such that periodicities along their short and long axes are 160 and 320 nm, respectively. (b) Traces of transmission minimums for the indicated polarization states of light subsequent to the application of 1 ms laser pulses with varying powers. (c) Dark-field microscope images of the studied geometry before ignition for the indicated polarizations. Similar to absorption, light scattering by elliptical particles is also highly dependent on polarization. (d) Dark-field images before and after raster-scanning the array with vertically polarized pulses. Initially, the structure looks uniform for the indicated polarization. After scanning, ignited particles, which have their long axes oriented vertically, display reduced scattering. (e) SEM image showing the selective ignition of vertically oriented particles. (f–h) Similar selective ignition experiments with a different sample. Here, a single laser pulse is applied. Decreased distance between similarly oriented particles allows the lowering of the threshold power.

expected based on their similar absorption at 532 nm (Figure 3c). The nonuniform trend of the ignition performance with particle size highlights the fact that in the considered size regime, the absorbed power is a more relevant factor than the particle size in determining the ignition behavior, providing a new perspective on previous studies that focused on correlating the ignition properties to the NP size.[18,34]

When a Gaussian laser beam is absorbed in the near-surface region of a material, it results in a well-defined temperature distribution that follows from a solution of the heat equation.[35,36]

DOI: 10.1021/acs.nanolett.7b04739
Nano Lett. 2018, 18, 1699–1706

For the dense array ($d \ll w$) of metal NPs placed on the glass substrate, this thermal solution is expected to provide valuable intuitive and quantitative insights into the heating process. A closed-form expression can be found for the steady-state temperature distribution on the sample surface during continuous heating as $T = T_{max} \exp\left(-\frac{1}{2}R^2\right) I_0\left(\frac{1}{2}R^2\right)$ with R the previously mentioned normalized radius r/w. In the center of the illumination spot, a maximum temperature is given by $T_{max} = fP/(2\sqrt{\pi K w})$, where f is the fraction of the absorbed power and K is the glass thermal conductivity. Remarkably, this simple equation for T_{max} matches qualitatively to the findings for uniformly illuminated NP arrays[37] and quantitatively to the T_{max} for a dense NP array illuminated by a Gaussian beam much larger than NP diameter.[5] The fact that $T_{max} \propto f$ highlights the critical role of LSPRs in controlling the ignition behavior as they allow one to directly tailor and engineer f.[1] The time to reach the steady state distribution is determined by the specific heat capacity of the substrate C, the beam radius, the volumetric mass density ρ, and the thermal conductivity as $\tau = Cw^2\rho/K$. For the borosilicate glass with a $C = 750$ J/kg·K and $\rho = 2.2 \times 10^3$ kg/m^3, the time to reach steady state is predicted to be 2.2 μs and in our experiments the turn-on time of our laser pulse limits the heating time to ~0.5 ms as seen in Figure 1d.

The analytical expression for the thermal distribution allows us to determine the spatial distribution of the heating rate throughout the pulse, assuming that the spatial distribution matches the steady-state result while the peak temperature follows the relatively slow rise of the laser power. From this data, we can estimate the size of the area in which the heating rate is sufficiently rapid to lead to the removal of NP via MDM if we assume that all NPs that reach the melting temperature of Al are removed. Figure 3a shows how the size of the ignited area depends on illumination power for the array of 160 nm diameter NPs under these assumptions. The red curve shows the predicted diameter as derived from the analytic model for the temperature distribution discussed above. Assuming a value of $K = 4$ W/(m·K), which is of a similar magnitude as the room-temperature literature value,[38] and magnitudes of $w = 2.2$ μm and $f = 0.43$, we find good agreement between theory and experiment for low illumination powers. For powers above 150 mW, the model predicts a larger ignited area than is seen in experiments. This has several identifiable reasons. First, the predicted area approaches the finite size of the patterned particle array. Second, at high temperature the effective thermal conductivity can increase due to radiative contributions.[39] Nevertheless, when we consistently use the same thermal conductivity value as above, this simple steady-state model displays remarkable agreement with experimental results for all particle arrays (Figure S7). As such, it affords a clear, intuitive understanding for the dependence of the MDM ignition zone diameter on illumination conditions, NP absorptivity, and substrate thermal properties.

To verify the validity of the steady-state thermal distribution, finite-element heat transfer simulations were carried out (COMSOL). The numerically simulated thermal distribution in the insets of Figure 3b, shows excellent quantitative agreement with the estimated temperature profile in the inset of Figure 3a (see Figure S7 for all results). The simulations show how individual Al NPs can serve as localized heat sources that produce a Gaussian-like temperature profile with a width that well-exceeds the interparticle spacing. This observation further justifies the simplifying assumption made in our analytical model that the discrete nature of the NP heat sources can be ignored. We also simulated temperature profiles for the different optical powers used in the experiments (Figure 3b). The temperature profile for a critical power of $P_c = 43$ mW (light green line) shows that this power is sufficient to reach a temperature equal to 933 K at the center of illumination spot. At lower powers, the melting temperature is not reached. This explains why we do not see a removal of NPs by the MDM. For higher powers, the modeled temperature curves show a nonlinear increase in the diameter within which the melting temperature of Al is reached. This explains the nonlinear increase in the size of the region ignited via the MDM.

The evolution of the transmission minimum of a NP array as we step up the laser power has been shown to critically depend on its plasmon-resonant properties (Figure 2f). This dependence can now be well-quantified in light of the new measurements (Figure 3a and Figure S7) by defining a threshold laser power required for driving ignition via the MDM. We define this threshold as the average of the first (i.e., lowest) laser power yielding a nonzero ignition diameter and the power before it. Figure 3c shows an obvious correlation between the threshold power and the absorbance of the NP array; a stronger absorption results in a lowered threshold. In this submicron size-regime, we do not find an obvious correlation between the particle size and the threshold power, confirming earlier theoretical predictions.[18] This suggests a clear route for controlling the MDM by leveraging decades of knowledge on particle absorption engineering from the plasmonics field.

In the plasmonics literature, the strongly polarization-dependent absorption of elliptical metal NPs is well-established.[40] Figure 4a shows the absorbance of an Al NP array with 125 nm long and 50 nm wide particles spaced at a period of 160 and 320 nm along their width and length, respectively. It is clear that the amount of absorbed power is very different when the array is illuminated with a 532 nm pump laser with the electric field polarized along the short or long axis of the ellipsoids. This suggests that the threshold powers for ignition could be very different as well. To test this point, we analyzed the dependence of the light transmission through arrays of elliptical particles on pump power for both polarization states. As expected, Figure 4b shows that when the light is polarized along the long axis (high absorption), less laser power is needed to render the sample transparent (blue curve) than for the case light is polarized along the short axis (green curve).

The dissimilar ignition power thresholds for the two orthogonal polarizations can be exploited to achieve submicron spatial control of ignition. To explore this point, we raster-scan a 350 mW, vertically polarized laser beam with a pulse duration of 1 ms and repetition rate of 10 Hz across particle arrays with horizontally- and vertically oriented NPs. Figure 4c–e illustrates this concept for an "S" pattern written with vertically oriented NPs, surrounded by horizontally oriented NPs, where vertical and horizontal refers to the orientation of the long axis in the image. Figure 4c shows the distinct optical response of the NP arrays in dark-field microscope images for the two orthogonal polarizations. Selective ignition of just the vertically oriented NPs is observed (see Figure 4d,e). Figure 4f–h shows the same idea for interlaced arrays of horizontal and vertical particles. Here, a lower power of 290 mW was sufficient to ignite the vertical particles based on a smaller interparticle spacing.

Conclusions. In this work, we show the photothermal heating of Al NPs beyond the Al melting temperature and the resulting ignition of NPs by the MDM. It is demonstrated that the MDM ignition threshold is critically dependent on the

DOI: 10.1021/acs.nanolett.7b04739
Nano Lett. 2018, 18, 1699–1706

absorbed power. This observation affords unprecedented levels of control over Al NP ignition. Such control was demonstrated for NPs of different size and orientation. Submicron spatial control over ignition at the few particle level was demonstrated as well. It is expected that the methods and effects described here can be applied to different, more complex particle geometries and arrangements. These general concepts can also be applied to reactive NPs made from a wide range of energetic materials that feature optical resonances. Metal nanoenergetic materials are known to have a great potential in applications including but not limited to nanofluids, nanogels, explosives, solid propellants, nanothermites, bonding and welding, microignition and fast initiation, material synthesis and processing, microactuation and propulsion, and biomedicine.[34,41] We anticipate that knowledge derived from the plasmonics field can facilitate advancements in such fields and also enable novel applications utilizing metal nanoenergetics.

Materials and Methods. *Sample Preparation.* The 50 nm thick silicon nitride film substrate used in sample preparation is available from Ted Pella, Inc. with the product code 21509-10. The optically thick glass substrate is a Fisherbrand (Fisher Scientific) borosilicate square cover glass with a thickness ranging between 0.17 and 0.25 mm. First, the substrates are submerged in acetone for 20 min, then rinsed with methanol and isopropanol (IPA) followed by drying under flowing nitrogen gas and cleaning with ultraviolet ozone plasma for 5 min. A bilayer electron beam (e-beam) sensitive resist process is employed by first spin coating 495 PMMA A4 (Microchem) for 40 s at 2000 rpm (target thickness 200 nm) and prebaking at 180 °C for 8 min. Afterward, spin coating of 950 PMMA A2 (Microchem) is performed at 2000 rpm (target thickness 100 nm) for 40 s followed immediately by prebaking at 180 °C for 3 min. Then, a thin layer (∼15 nm) of Espacer 300Z (Showa Denko) is spin coated at 3000 rpm for 40 s to prevent charging. The desired patterns are written with a JEOL JBX-6300FS e-beam lithography system at 100 kV acceleration voltage. Afterward, Espacer 300Z is cleaned with deionized water and the e-beam resists are developed for 40 s in a 1:1 MIBK/IPA solution. Subsequently, 5 nm titanium and 70 nm aluminum thin films are deposited with an Innotec ES26C e-beam evaporator system at $\sim 7 \times 10^{-7}$ Torr chamber pressure. Finally, a multistep lift-off process is used. First, samples are soaked in Remover PG (Microchem) for 20 min at 60 °C. Then, acetone spraying by inducing shear force is performed for 3 min. A final acetone soak for 5 min, an IPA rinse, and nitrogen drying completes the sample preparation.

Ignition Experiments. The laser beam (λ_0 = 532 nm) is generated by a frequency-doubled Spectra Physics Millennia Pro 5sJS continuous wave laser. The fundamental frequency at λ_0 = 1064 nm is removed by a Thorlabs FL532-10 bandpass filter. The laser polarization is purified with a Thorlabs LPVISE100-A linear polarizer. Afterward, the laser beam goes through a Thorlabs EO-AM-NR-C4 electro-optic amplitude modulator. The electrical input of the modulator is connected to a Thorlabs HVA200 high-voltage amplifier, which is driven by a Hewlett-Packard 8015A pulse generator. After the modulator, a Thorlabs GTH5M-A linear polarizer with its transmission axis rotated by 90° with respect to the previous polarizer is employed to enable the modulation of the laser beam. A Thorlabs WPMH10M-532 half-wave plate is used to control the polarization angle of the light. Then, the beam is split into two paths by a Thorlabs BS010 50:50 nonpolarizing beam splitter. One of the beams is used for measuring the laser power utilizing an Ophir Nova II optical power meter. The other beam is focused onto the sample with an Olympus RMS10X (NA = 0.25, WD = 10.6 mm) objective.

Electron Microscopy. SEM analysis is performed using a FEI Magellan 400 XHR microscope. The microscope is operated at an acceleration voltage of 5 kV and a working distance of 4 mm. Spin coating of Espacer 300Z (Showa Denko) prior to imaging reduces the undesired charging effect.

The EDS measurements are performed with an image-corrected FEI Titan TEM. The microscope is operated in STEM mode at an acceleration voltage of 80 kV and is equipped with an Oxford X-max silicon drift detector. The EDS acquisition is performed in the 0−20 keV spectral range with a pixel time of 0.5 ms, providing a frame time of 32.8 s (256 × 256 resolution). Typically, 20−25 frames are acquired for accurate elemental quantification. To enhance X-ray detection, the sample is titled 15°. The data acquisition and analysis is performed using the INCA software from Oxford Instruments. The Cliff-Lorimer ratio method of the K lines is used for elemental quantification. It is conservatively estimated that the resulting elemental quantification accuracy is ±20%. Typically, the accuracy is less for the lighter element O (i.e., closer to ±20%) and better for the heavier element Al (i.e., less than ±20%).

Cross-section STEM imaging is performed following gallium focused ion beam (FIB, FEI Versa3D) "lift-out" of a thin foil section from the surface of a borosilicate substrate near the center of an ignition region for an aluminum nanoparticle array. This is accomplished by depositing a rectangle of platinum using ion beam induced deposition (IBID) of platinum to protect the surface region. Triangular cross-section trenches are then patterned by FIB on either side of the platinum bar to produce a wall, using ion beam currents of 5−65 nA at 30 kV. A small section of the wall is attached to a micromanipulator by IBID platinum. This section is then removed and reattached to a copper support substrate (Ted Pella). Final thinning was conducted via the FIB at 30 kV using currents between 0.3 and 1 nA. The section is imaged in electron beam STEM mode at 30 kV (FEI Versa3D) with bright-field, low-angle annular dark-field, and high-angle annular dark-field detectors.

Infrared Thermal Imaging. Thermal light emerging from the sample is collected with a Thorlabs LMM-40X-P01 40× reflective objective (NA = 0.5) and focused onto a FLIR SC4000 infrared camera. A frame rate of 4848.7 Hz with an integration time of 200 μs is used to record the laser-induced ignition event on a 50 nm silicon nitride membrane. Afterward, the same sample is heated to several different temperatures using a Linkam THMSE600 temperature controlled stage and the resulting thermal light is recorded with the same integration time. These images are then used to convert the photon counts obtained from the camera into absolute temperatures.

Optical Simulations. Optical simulations are performed using the commercially available software FDTD Solutions from Lumerical Solutions, Inc. Further details about simulations are provided in the legend of Figure S4.

Optical Characterization. Measurements are conducted with a Nikon C1 confocal microscope coupled to a Pixis 1024B charge coupled device camera through an Acton SpectraPro 2300i spectrometer. Samples are illuminated from the substrate side with a broadband halogen lamp through a condenser lens with NA = 0.8. The transmitted light is collected by a Nikon LU Plan Fluor BD 50× bright-field/dark-field objective (NA = 0.8, WD = 1 mm) in the bright-field arrangement. A pinhole diameter of 150 μm is used for the confocal scanner. The light is then coupled to a Thorlabs BFH48-600 multimode fiber (NA = 0.48, 600 μm core

DOI: 10.1021/acs.nanolett.7b04739
Nano Lett. 2018, 18, 1699−1706

diameter) and transferred to the spectrometer. We estimate the collection area has a diameter of approximately 12 μm.

Thermal Simulations. Thermal simulations are performed using the commercially available software COMSOL Multiphysics from COMSOL, Inc. Further details about simulations are provided in the legend of Figure S7.

■ ASSOCIATED CONTENT

Supporting Information

The Supporting Information is available free of charge on the ACS Publications website at DOI: 10.1021/acs.nanolett.7b04739.

Optical and thermal modeling of the studied structures, additional electron microscope images visualizing a postignition cross-section and comparing fast ignition to a slow one, atomic force microscope analysis of an ignition region, and complete transmission spectra of studied samples (PDF)

■ AUTHOR INFORMATION

Corresponding Author

*E-mail: brongersma@stanford.edu.

ORCID

Søren Raza: 0000-0002-0296-7202

Xiaolin Zheng: 0000-0002-8889-7873

Mark L. Brongersma: 0000-0003-1777-8970

Author Contributions

M.M., J.-H.K., and M.L.B. conceived the idea of studying the ignition behavior of lithographically defined metal nanoparticles. M.M. and J.-H.K. performed the ignition experiments. M.M. performed the electromagnetic simulations. S.R. and D.S. performed the electron microscopy. All authors contributed to analyzing the data and the writing of the manuscript. The project was supervised by M.L.B.

Notes

The authors declare no competing financial interest.

■ ACKNOWLEDGMENTS

This work acknowledges support from the Department of Energy Grant DE-FG07-ER46426. S.R. was supported by a research grant (VKR023371) from VILLUM FONDEN. Part of this work was performed at the Stanford Nano Shared Facilities (SNSF). We also acknowledge valuable discussions with Dr. Yuma Ohkura at the start of the project.

■ REFERENCES

(1) Hutter, E.; Fendler, J. H. *Adv. Mater.* **2004**, *16*, 1685−1706.

(2) Baffou, G.; Quidant, R. *Laser and Photonics Reviews* **2013**, *7*, 171−187.

(3) Govorov, A. O.; Richardson, H. H. *Nano Today* **2007**, *2*, 30−38.

(4) Baffou, G.; Quidant, R.; García De Abajo, F. J. *ACS Nano* **2010**, *4*, 709−716.

(5) Baffou, G.; Berto, P.; Bermúdez Ureña, E.; Quidant, R.; Monneret, S.; Polleux, J.; Rigneault, H. *ACS Nano* **2013**, *7*, 6478−6488.

(6) Boyer, D.; Tamarat, P.; Maali, A.; Lounis, B.; Orrit, M. *Science (Washington, DC, U. S.)* **2002**, *297*, 1160−1163.

(7) Boulais, E.; Lachaine, R.; Hatef, A.; Meunier, M. *J. Photochem. Photobiol., C* **2013**, *17*, 26−49.

(8) Ghosh, P.; Han, G.; De, M.; Kim, C. K.; Rotello, V. M. *Adv. Drug Delivery Rev.* **2008**, *60*, 1307−1315.

(9) Jain, P. K. K.; El-Sayed, I. H. H.; El-Sayed, M. A. A. *Nano Today* **2007**, *2*, 18−29.

(10) Kim, J. *Lab Chip* **2012**, *12*, 3611.

(11) Li, Y.; Verbiest, T.; Strobbe, R.; Vankelecom, I. F. J. *J. Mater. Chem. A* **2014**, *2*, 3182−3189.

(12) Qiu, J.; Wei, W. D. *J. Phys. Chem. C* **2014**, *118*, 20735−20749.

(13) Zhang, W.; Li, Q.; Qiu, M. *Opt. Express* **2013**, *21*, 172−181.

(14) Dreizin, E. L. *Prog. Energy Combust. Sci.* **2009**, *35*, 141−167.

(15) Rossi, C.; Estève, D. *Sens. Actuators, A* **2005**, *120*, 297−310.

(16) Rai, A.; Park, K.; Zhou, L.; Zachariah, M. R. *Combust. Theory Modell.* **2006**, *10*, 843−859.

(17) Chowdhury, S.; Sullivan, K.; Piekiel, N.; Zhou, L.; Zachariah, M. R. *J. Phys. Chem. C* **2010**, *114*, 9191−9195.

(18) Levitas, V. I.; Asay, B. W.; Son, S. F.; Pantoya, M. *J. Appl. Phys.* **2007**, *101*, 083524.

(19) Levitas, V. I.; Asay, B. W.; Son, S. F.; Pantoya, M. *Appl. Phys. Lett.* **2006**, *89*, 071909.

(20) Levitas, V. I.; Pantoya, M. L.; Dean, S. *Combust. Flame* **2014**, *161*, 1668.

(21) Levitas, V. I. *Combust. Flame* **2009**, *156*, 543−546.

(22) Granier, J. J.; Pantoya, M. L. *Combust. Flame* **2004**, *138*, 373−383.

(23) Yang, Y.; Sun, Z.; Wang, S.; Dlott, D. D. *J. Phys. Chem. B* **2003**, *107*, 4485−4493.

(24) Ohkura, Y.; Rao, P. M.; Zheng, X. *Combust. Flame* **2011**, *158*, 2544−2548.

(25) Abboud, J. E.; Chong, X.; Zhang, M.; Zhang, Z.; Jiang, N.; Roy, S.; Gord, J. R. *Appl. Phys. Lett.* **2013**, *102*, 023905.

(26) Knight, M. W.; King, N. S.; Liu, L.; Everitt, H. O.; Nordlander, P.; Halas, N. J. *ACS Nano* **2014**, *8*, 834−840.

(27) Park, K.; Lee, D.; Rai, A.; Mukherjee, D.; Zachariah, M. R. *J. Phys. Chem. B* **2005**, *109*, 7290−7299.

(28) Lima, M. M.; Monteiro, R. *Thermochim. Acta* **2001**, *373*, 69−74.

(29) Shiu, T.-R.; Grigoropoulos, C. P.; Cahill, D. G.; Greif, R. *J. Appl. Phys.* **1999**, *86*, 1311.

(30) Parsons, J.; Hendry, E.; Burrows, C. P.; Auguié, B.; Sambles, J. R.; Barnes, W. L. *Phys. Rev. B: Condens. Matter Mater. Phys.* **2009**, *79*, 073412.

(31) Scholze, H. *Glass: Nature, Structure, and Properties*; Springer-Verlag, 1991.

(32) Haynes, C. L.; McFarland, A. D.; Zhao, L.; Van Duyne, R. P.; Schatz, G. C.; Gunnarsson, L.; Prikulis, J.; Kasemo, B.; Käll, M. *J. Phys. Chem. B* **2003**, *107*, 7337−7342.

(33) Hao, F.; Larsson, E. M.; Ali, T. A.; Sutherland, D. S.; Nordlander, P. *Chem. Phys. Lett.* **2008**, *458*, 262−266.

(34) Yetter, R. A.; Risha, G. A.; Son, S. F. *Proc. Combust. Inst.* **2009**, *32*, 1819−1838.

(35) Lax, M. *J. Appl. Phys.* **1977**, *48*, 3919−3924.

(36) Lax, M. *Appl. Phys. Lett.* **1978**, *33*, 786−788.

(37) Govorov, A. O.; Zhang, W.; Skeini, T.; Richardson, H.; Lee, J.; Kotov, N. A. *Nanoscale Res. Lett.* **2006**, *1*, 84−90.

(38) Assael, M. J.; Gialou, K.; Kakosimos, K.; Metaxa, I. *Int. J. Thermophys.* **2004**, *25*, 397−408.

(39) Viskanta, R.; Song, T.-H. *Glas. Berichte* **1985**, *58*, 80.

(40) Kreibig, U.; Vollmer, M. *Optical Properties of Metal Clusters*; Springer-Verlag, 1995.

(41) Zhou, X.; Torabi, M.; Lu, J.; Shen, R.; Zhang, K. *ACS Appl. Mater. Interfaces* **2014**, *6*, 3058−3074.

DOI: 10.1021/acs.nanolett.7b04739
Nano Lett. 2018, 18, 1699−1706